Origin of the Resistance-Area-Product Dependence of Spin-Transfer-Torque Switching in Perpendicular Magnetic Random-Access Memory Cells

G. Mihajlović,[*] N. Smith, T. Santos, J. Li, M. Tran, M. Carey, B.D. Terris, and J.A. Katine[†]

Western Digital Research Center, Western Digital Corporation, San Jose, California 95119, USA

We report on an experimental study of current-induced switching in perpendicular magnetic random-access memory (MRAM) cells with variable resistance-area products (RAs). Our results show that in addition to spin-transfer torque (STT), current-induced self-heating and voltage-controlled magnetic anisotropy also contribute to switching and can explain the RA dependencies of the switching-current density and STT efficiency. Our findings suggest that thermal optimization of perpendicular MRAM cells can result in significant reduction of switching currents.

I. INTRODUCTION

As information technology enters a new era [1], with the Internet of Things expected to connect over 30 billion devices, generating vast amounts of data that need to be processed and stored [2], there is a rapidly growing demand for faster, denser, and more power-efficient nonvolatile memories [3] that could be organized in alternative hierarchies offering better system performance and greater functionality [4], all preferably at lower cost. Spin-transfer-torque magnetoresistive random-access memory (STT MRAM) [5,6] is uniquely positioned to address this challenge, as it is the only emerging memory that could combine the high speed and endurance of static random-access memory (SRAM), the high density of DRAM, and the nonvolatility of flash [7]. The heart of the MRAM cell is the magnetic tunnel junction (MTJ), which provides the write, read, and bit-storage functionality, essentially using two magnetic layers, the reference layer (RL) and the free layer (FL), separated by a magnesium-oxide (MgO) tunnel barrier [5,7]. The two bit-storage states are the parallel (P) and antiparallel (AP) magnetization orientations of the FL relative to the RL, distinguished by different resistance-area products (RAs) of the MTJ: $(RA)_P \equiv$ RA for the P state and $(RA)_{AP} = (1 + TMR)RA$ for the AP state, where TMR is the tunneling magnetoresistance ratio.

For RL and FL with perpendicular magnetic anisotropy (PMA), the STT critical $P \rightleftharpoons AP$ switching voltage V_{c0} (defined at zero temperature and for infinitely long time) is, in the macrospin approximation [8], expressible in terms of

a spin-torque field H_{ST} and torquence τ as

$$\alpha H_k = \pm H_{ST} = \pm \tau V_{c0}/\text{RA}, \quad \tau = \frac{\hbar}{2e} \frac{\eta}{M_s t}, \quad (1)$$

where α, M_s, t, and H_k are the damping parameter, saturation magnetization, thickness, and net PMA field of the FL, respectively, and $\eta = \sqrt{\text{TMR}(\text{TMR} + 2)}/[2(\text{TMR} + 1)]$ is a polarization efficiency factor. Apart from a minor RA dependence of η, due to TMR being a weak function of RA (see Table I), the critical current density $J_{c0} \equiv V_{c0}/\text{RA}$ is not expected to depend on RA. Experimentally, however, an RA dependence has been observed by several groups [9–12] and attributed [10,12] to an RA-dependent spin-pumping [13] contribution to α in Eq. (1). Here, we show that the RA dependence of J_{c0} is influenced by other phenomena, in particular the current-induced self-heating of an MRAM cell, which reduces the effective H_k of the FL, and, to a smaller extent, the voltage-controlled magnetic anisotropy effect (VCMA) [14,15]. As the temperature rise of the FL is proportional to the dissipated power density [16] $\text{RA}J^2$, higher-RA devices result in lower J_{c0}. In addition, as the VCMA effect is proportional to the bias voltage V_b across the MRAM cell, for a given J, the VCMA effects are stronger with a higher RA. The combination of heating and VCMA quantitatively explains all of our experimental findings, in particular the much stronger RA dependence of J_c for P-to-AP switching (P → AP) compared to AP → P, and the RA dependence of the STT efficiency E_b/I_{c0} obtained from pulse-width t_p dependent measurements of the switching voltage V_c in the thermally activated (TA) regime [17,18] (E_b is the energy barrier for magnetization reversal of the FL and $I_{c0} \equiv V_{c0}/R_P$ is the critical switching current).

---

[*]goran.mihajlovic@wdc.com
[†]jordan.katine@wdc.com

II. DEVICE FABRICATION

The MRAM film stacks used in this study consist of a Ta/Pt seed layer (8.0 nm), a (Co/Pt)/Ru/(Co/Pt)/Co-Fe-B synthetic antiferromagnet RL (7.1 nm), a MgO tunnel barrier, a Co-Fe-B/Co-Fe/W/Co-Fe FL (2.1 nm), a MgO cap layer for enhancing H_k, and a Ru/Ta cap layer (3 nm). The films are deposited by magnetron sputtering in an Anelva C-7100 system and then annealed at $335\,°C$ for 1 h. The MgO layers are rf sputtered from a MgO target. The RA and TMR values measured on the annealed films by current-in-plane tunneling (CIPT) [19] are shown in Table I. Variation of the RA values in the range $5–20\,\Omega\,\mu m^2$ is achieved by adjusting the sputter time of the MgO barrier and, consequently, the TMR ratio increases from 133 to 156%, respectively. For this range of RA values, $M_s t$ measured by vibrating-sample magnetometry, as well as the H_k and α of the FL measured by full-film ferromagnetic resonance (FMR), are identical (see Table I).

Circular MRAM test-device cells are fabricated using 193-nm-deep UV optical lithography, followed by reactive ion etching of a hard mask, ion milling of the MRAM film, SiO_2 refill, and chemical-mechanical planarization. The median electrical-device diameters D, determined by fitting R_P vs RA for the given optical mask size, are approximately 120, 100, 80, and 60 nm. A transmission-electron-microscopy (TEM) image of a representative device is shown in Fig. 1(a). Figure 1(c) shows R vs the perpendicular external magnetic field H for an MRAM cell with RA $= 10\,\Omega\,\mu m^2$ (RA10) and $D \cong 60$ nm measured at constant $V_b = 50$ mV, showing TMR $\cong 140\%$, a coercive field $H_c = (H_{sw}^{P\to AP} - H_{sw}^{AP\to P})/2 \cong 2$ kOe (where H_{sw} is the switching field), and an offset field $H_{offs} = (H_{sw}^{P\to AP} + H_{sw}^{AP\to P})/2 \cong 300$ Oe that favors the P state. Figure 1(d) shows R vs V_b. One can see that P $\to$ AP and AP $\to$ P occur at $V_c^{P\to AP} = -0.54$ V and $V_c^{AP\to P} = +0.58$ V, respectively.

III. RESULTS AND ANALYSIS

Figure 1(b) shows $J_c = I_c/(D^2\pi/4)$, determined by ramping V_b with a dwell time of approximately 10 ms and

TABLE I. The transport and magnetic properties of the free-layer films used in this study. The parameter values are expressed to the last significant digit based on the corresponding error analysis, except for α, where the absolute error is 0.0003.

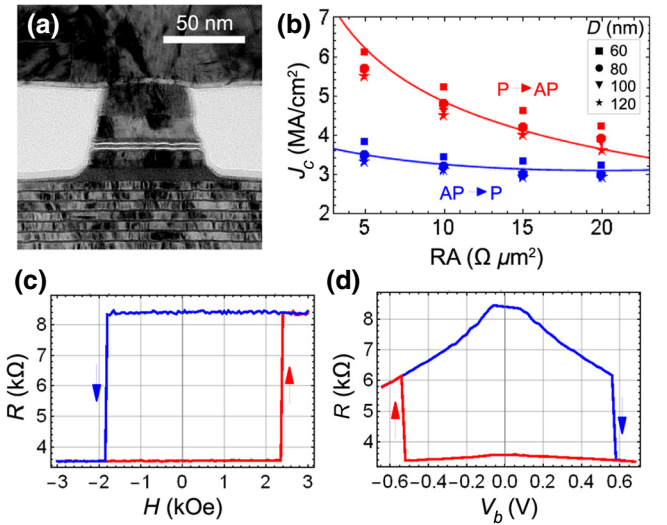| RA ($\Omega\,\mu m^2$)	TMR (%)	$M_s t$ (memu/cm^2)	H_k (kOe)	α
5	133	0.232	2.71	0.0100
10	147	0.227	2.72	0.0102
15	156	0.226	2.69	0.0100
20	156	0.232	2.69	0.0094

FIG. 1. (a) A TEM image of an MRAM cell used in this study. The two white lines correspond to the two MgO barriers. The RA of the cell is dominated by the bottom barrier. The top barrier provides additional PMA but its contribution to the total RA of the cell is less than $1\,\Omega\,\mu m^2$, as determined by CIPT measurements for the MgO cap thickness used in this study and data fitting by the double-barrier model [20]. In our analysis, the total RA of the cell is used. (b) The measured J_c vs RA (symbols) and calculated (lines) using fit-parameter values described in the text. Each J_c data-point value is a median from >500 devices. Due to the large sample size, the standard error of the median for each data point is less than 0.5% and within the data points. The measured (c) R vs H and (d) R vs V_b of an MRAM cell with RA10.

measuring the current I_c just before switching, as a function of RA. J_c decreases with an increasing RA for both AP $\to$ P and P $\to$ AP. The dependence, however, is much stronger for the latter, with J_c decreasing by approximately 50% from RA5 to RA20, while for AP $\to$ P the decrease is only approximately 15%. Also, J_c at a given RA increases with a decreasing D. This is contrary to what one would expect in the TA-switching regime of these measurements, as smaller devices are more thermally unstable.

The change in J_c with RA cannot be attributed to an RA-dependent spin-pumping [13] contribution to α, as our film FMR measurements show that α is independent of RA (see Table I). It also cannot be explained by any dependence of M_s or H_k of the FL on RA, as they are also measured to be RA independent (Table I). In order to understand the origin of these dependencies, we perform additional R vs H measurements as a function of V_b.

Figure 2(a) shows representative R vs H data for different V_b from a single cell. V_b is varied from -0.95 V (bottom curve) to $+0.95$ V (top curve) in 0.1 V steps. The obtained V_b dependencies of H_{sw} for P $\to$ AP and AP $\to$ P and of H_{offs} and H_c are shown in Figs. 2(b), 2(c), and 2(d), respectively. While the near-linear V_b dependence of H_{offs} shown in Fig. 2(c) is close to what is
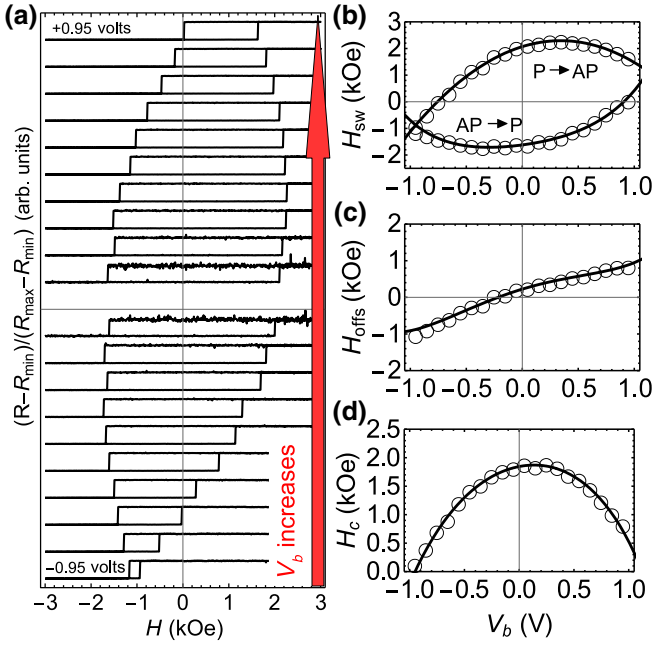
FIG. 2. (a) R vs H for -0.95 V $< V_b <$ $+0.95$ V for a MRAM cell with RA20 and $D = 80$ nm. The R-H transfers in the center are noisiest, as they are measured at the lowest V_b. (b) H_{sw}, (c) H_{offs}, and (d) H_c vs V_b obtained from the measurements shown in (a) (symbols) and the corresponding dependencies calculated using Eqs. (2) and (3) (lines), with $H_{c0} = 1.85$ kOe, $H_{RL} = 225$ Oe, $\tau/\alpha = 18.6$ kOe μm^2/A, $\epsilon = 0.37$ kOe/V, and $\zeta = 37.8$ kOe μm^2/W.

expected from STT [8], Fig. 2(d) shows that H_c exhibits a quadratic component of V_b dependence that strongly suggests self-heating. Indeed, in the macrospin approximation [8], STT alone predicts no dependence of H_c on V_b. A more careful inspection of Fig. 2(d) shows that H_c also exhibits a smaller linear component of V_b dependence, which could be due to VCMA.

Alternatively, the V_b dependence of H_k can be measured more directly (see Fig. 3) from device-level thermally induced FMR (mag-noise) spectra [21]. The expected peak-resonance frequency $f_0 \approx \gamma$ $\sqrt{\left[(H_k \pm H_z)^2 + H_{ST}^2\right]\left[1 - (H_y/H_k)^2\right]}$, where $\gamma \cong 3$ GHz/kOe is the gyromagnetic ratio, H_y and H_z are the total in-plane and perpendicular magnetic fields, respectively, and $H_{ST} = (\alpha H_k)(V_b/V_{c0})$ [see Eq. (1)]. For the measurements in Fig. 3 (near the AP state), $V_b < V_{c0}$; thus H_{ST} is negligible, $H_z \approx 0$, and $H_y \cong 1$ kOe $\ll f_0/\gamma$ makes only a small correction to H_k. As shown in Fig. 3 for an RA20 cell, $f_0(V_b)$ has both a quadratic and linear (VCMA) contributions, the latter more clearly visible than is indicated by H_c vs V_b shown in Fig. 2(d). A similar dependence of the magnetic anisotropy energy on V_b has been reported recently by Goto *et al.* [22] and has also been attributed to current-induced self-heating. One
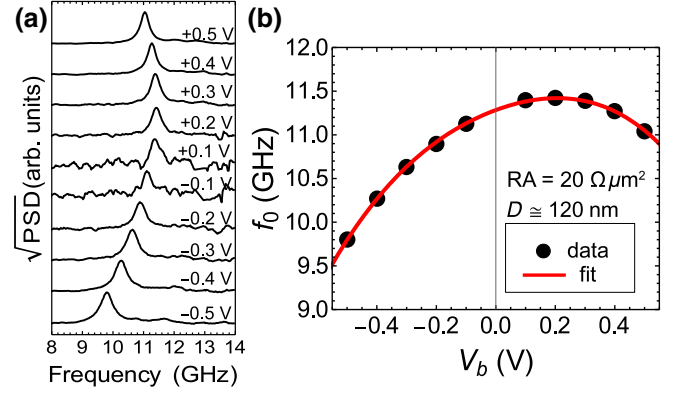
can fit this dependence by expressing $H_k = H_{k0} + \epsilon V_b - \zeta V_b^2/\text{RA}'$, where $\text{RA}' = \text{RA}(1 + \text{TMR}|_{V_b=0})(1 - 0.5|V_b|)$ is the approximate expression for V_b-dependent RA in the AP state [see Fig. 1(d)]. The values obtained are $H_{k0} = (3.76 \pm 0.01)$ kOe, $\epsilon = (0.42 \pm 0.01)$ kOe/V, and $\zeta = 44.0 \pm 0.5$ kOeμm^2/W. The sign of the VCMA is positive, i.e., it increases H_k for positive V_b (AP $\rightarrow$ P polarity).

Having established that VCMA and self-heating are present, $H_{sw}(V_b)$ is explicitly expressed as

$$H_{sw}^{P\rightarrow AP} = H_{c0} + H_{RL} + \frac{\tau}{\alpha}\frac{V_b}{\text{RA}} + \epsilon V_b - \zeta\frac{V_b^2}{\text{RA}}, \quad (2)$$

$$H_{sw}^{AP\rightarrow P} = -H_{c0} + H_{RL} + \frac{\tau}{\alpha}\frac{V_b}{\text{RA}} - \epsilon V_b + \zeta\frac{V_b^2}{\text{RA}'}, \quad (3)$$

where H_{RL} characterizes the perpendicular dipolar stray field from the reference layer and the following terms are from STT, VCMA, and self-heating effects, respectively.

Figures 4(a)–4(d) show *simultaneous* fits to $H_{sw}^{P\rightarrow AP}$ and $H_{sw}^{AP\rightarrow P}$ vs V_b for *all* RA values explored in this experiment. All data can be fitted with the same set of RA-*independent* parameters: $H_{c0} = (1.86 \pm 0.01)$ kOe, $H_{RL} = (244 \pm 3)$ Oe, $\tau/\alpha = (18.6 \pm 0.1)$ kOeμm^2/A, $\epsilon = (0.42 \pm 0.01)$ kOe/V, and $\zeta = (42.8 \pm 0.2)$ kOe μm^2/W.

One can now calculate V_c by solving Eqs. (2) and (3) for V_b for which $H_{sw} = 0$. Then $J_c^{P\rightarrow AP} = V_c^{P\rightarrow AP}/\text{RA}$ and $J_c^{AP\rightarrow P} = V_c^{AP\rightarrow P}/\text{RA}'(V_c^{AP\rightarrow P})$. The calculated J_c dependencies on RA using the RA-independent fit parameters are shown as lines in Fig. 1(b). The agreement is excellent for both P $\rightarrow$ AP and AP $\rightarrow$ P. In particular, the model reproduces the much stronger RA dependence of J_c for P $\rightarrow$ AP.

The mild increase of J_c with a decreasing cell size shown in Fig. 1(b) is believed to result from more relative cell cooling via three-dimensional heat flow into

FIG. 3. (a) The normalized mag-noise root-mean-square power spectral density (PSD) measured for different V_b. (b) The resonance frequency f_0 vs V_b corresponding to the measurements shown in (a). The line is fitted to the data using a model that includes VCMA and self-heating contributions, as described in the text.
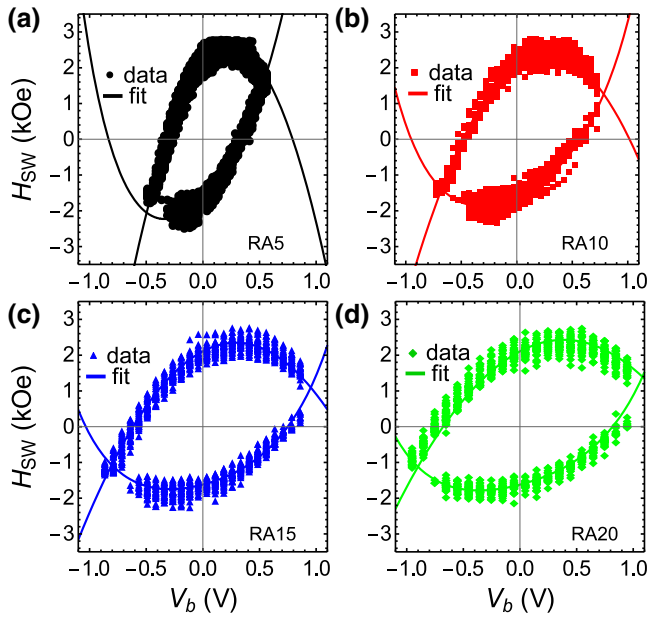
FIG. 4. H_{sw} vs V_b for different RA. The data on each plot are from all measured devices (approximately 40 in total) with $D = 60$–120 nm. The lines are fits to Eqs. (2) and (3) with simultaneous fit parameters.

FIG. 5. (a) The measured R vs H for different Ts for an MRAM cell with RA20, $D = 100$ nm. (b) H_c vs T for the data shown in (a) (symbols) and a linear fit (line) with slope $dH_c/dT \cong 10$ Oe/K. (c) FL T vs V_b determined for the P state for different RAs. (d) T vs the dissipated power density for different RAs. The line is a linear fit to the data, i.e., $T = T_0 + R_{th}AV_b^2/RA$ with $T_0 = (28 \pm 2)$ °C and $R_{th}A = (4.0 \pm 0.1)$ K μm^2/mW. Each data point in (c) and (d) is the median from approximately 25 measured cells averaged over $D = 60$, 80, 100, and 120 nm devices. The standard error of the median for each data point is less than 1% and is within the data points.

the surrounding encapsulation material, in addition to a weakly increasing H_{c0} with decreasing device size due to a reduced demagnetization field near the FL edges [23]. The deviation of H_{offs} from a linear dependence on V_b as shown in Fig. 3(c) arises from the differences in the self-heating terms in Eqs. (2) and (3) for P $\rightarrow$ AP and AP $\rightarrow$ P, respectively.

The value of $H_{k0} \cong 3.8$ kOe extracted from the FMR data of Fig. 3 is a factor of 2 larger than the value of $H_{c0} \cong 1.9$ kOe characteristic of the Fig. 4 data. The former is a passive measurement under quiescent macrospin conditions and should better represent the true device FL PMA compared to the latter, which likely involves a nucleated magnetization-reversal process [24] that does not resemble uniform macrospin rotation. In the macrospin picture [see Eq. (1)], $\tau/\alpha = H_{k0}/J_{c0} = (\hbar\eta)/(2e\alpha M_s t)$. Using Table I, one then estimates $\tau/\alpha \cong 65$ kOe μm^2/A. This is about 3.5 times larger than the value found from fitting the data in Fig. 4. More than half of this discrepancy may be ascribed to the aforementioned factor-of-2 difference between macrospin H_{k0} and H_{c0} obtained by fitting the same nonmacrospin data of Fig. 4 used to fit τ/α.

In order to determine how the cell temperature T depends on V_b, we perform R vs H measurements over T range 30–120 °C. Figures 5(a) and 5(b) show representative results obtained from a single cell. A typical value $dH_c/dT \cong 10$ Oe/K is obtained that is within 10% of the dH_k/dT found from thermal FMR measurements analogous to those shown in Fig. 3. The measured dH_c/dT
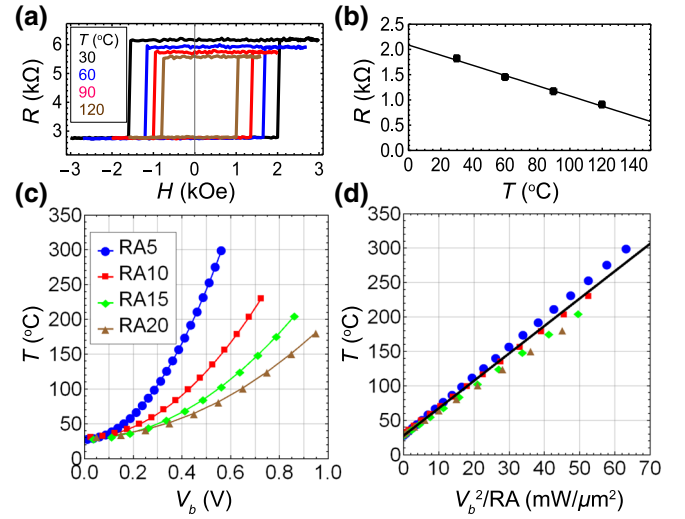
factors convert H_c vs V_b data into T vs V_b and T vs V_b^2/RA, as is illustrated in the figure and described in the caption.

We also measure V_c vs t_p in the range 10 ns to 5 ms and evaluate J_{c0}, the thermal stability factor $\Delta = E_b/k_BT$ (where k_B is the Boltzmann constant), and E_b/I_{c0} using the TA model [17,18]. Figure 6(a) shows an example of the data from a RA10 cell, which in the range $t_p \geq 5$ μs is fitted to the TA model $\ln[t_p/(\tau_0 \ln 2)] = \Delta_{eff} = \Delta(H_k/H_{k0})(T_0/T)$ using the following two forms:

$$H_k = H_{k0}\left(1 \pm \frac{V_c}{V_{c0}}\right), \quad T = T_0 \qquad (4)$$

(solid lines) and

$$H_k = H_{k0} \pm \frac{\tau}{\alpha}\frac{V_c}{RA} + \epsilon V_c - \zeta\frac{V_c^2}{RA'}, \quad T = T_0 + R_{th}A\frac{V_c^2}{RA'} \qquad (5)$$

(dashed lines), where $\tau_0 = 1$ ns is taken to be the inverse attempt frequency, H_{k0} and T_0 are H_k and T at $V_b = 0$, $R_{th}A$ is the effective thermal resistance-area product, and the $(+)$ and $(-)$ signs correspond to P $\rightarrow$ AP and AP $\rightarrow$ P, respectively. Equation (4) is commonly found in the literature [12,17,18], where only STT influence is accounted for, while Eq. (5) incorporates the additional V_b dependencies of H_k from both VCMA and self-heating, as well as the
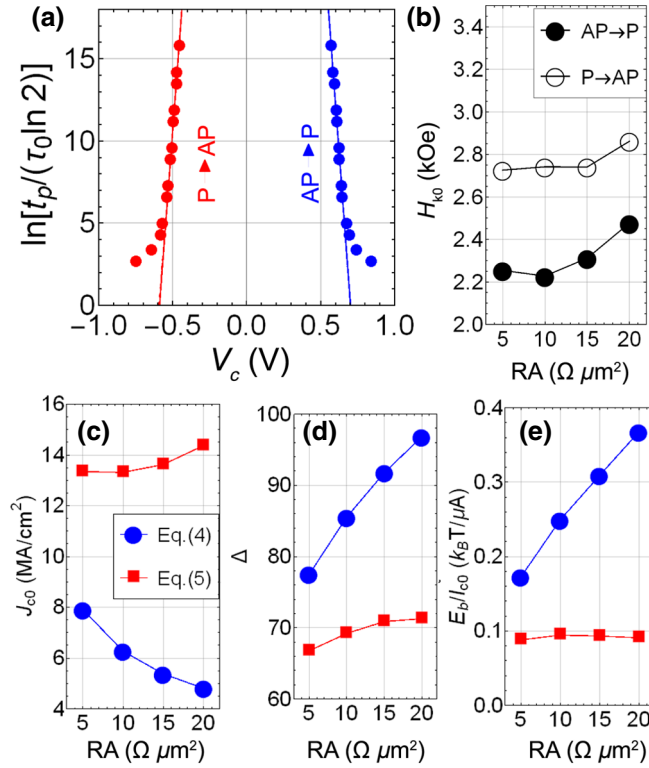
FIG. 6. (a) V_c vs $\ln\left[t_p/(\tau_0\ln 2)\right]$ values (symbols) measured on a RA10 device and fits to the TA model with H_k and T expressed using Eq. (4) (solid line) and Eq. (5) (dashed line). The fit lines are on top of each other and are indistinguishable. (b) H_{k0} values obtained by fitting the data as in (a) using Eq. (5). The RA dependence of (c) J_{c0}, (d) Δ, and (e) the STT efficiency obtained by fitting the data as in (a) to Eqs. (4) and (5). Each point in (b)–(e) is the median from approximately 30 measured cells averaged over $D = 60$, 80, 100, and 120 nm devices.

explicit V_b dependence of cell T, as described earlier via Eqs. (2) and (3) and Figs. 4 and 5. Along with the fit parameter Δ (both forms), Eq. (4) uses the second fit parameter V_{c0}. When using Eq. (5), H_{k0} is the only additional fit parameter, while the values for τ/α, ϵ, and ζ are those RA-*independent* parameter values determined from the data of Fig. (4), $T_0 = 303$ K, and $R_{th}A \cong 4$ K μm^2/mW is determined from data in Fig. 5. For Fig. 6(c), $J_{c0} = V_{c0}/RA$ for the Eq. (4) case and $J_{c0} = (\tau/\alpha)^{-1}H_{k0}$ for the Eq. (5) case. Note that, in both cases, the AP $\rightarrow$ P and P $\rightarrow$ AP branches are fitted separately and V_{c0} and Δ are determined as their average. One can see in Fig. 6(a) that both models fit the data well (the solid and dashed lines are indistinguishable).

Figure 6(b) shows H_{k0} values as a function of RA. We see that, as expected, H_{k0} is independent of RA with RA-averaged values $H_{k0}^{P\rightarrow AP} = (2.77 \pm 0.07)$ kOe and $H_{k0}^{AP\rightarrow P} = (2.32 \pm 0.12)$ kOe. These values are higher than the H_{c0} values obtained from the H-driven magnetization-reversal measurements described by Eqs. (2) and (3) (see

Figs. 2 and 4), but are lower than the H_{k0} values obtained in thermal FMR measurements that do not involve any magnetization reversal. This is not surprising considering the different magnetization excitation and reversal processes in these measurements. Note that the difference $\left(H_{k0}^{P\rightarrow AP} - H_{k0}^{AP\rightarrow P}\right)/2 \cong 220$ Oe agrees well with the value of H_{RL} obtained from fitting the data of Fig. 4.

Figures 6(c)–6(e) compare the RA dependencies of J_{c0}, Δ, and E_b/I_{c0}, obtained by fitting experimental data using Eqs. (4) and (5). We find strong RA dependencies of all those quantities when t_p-dependent V_c data are fitted to Eq. (4). In particular, we observe a large increase of E_b/I_{c0} with an increasing RA, similar to previous reports [11,12]. However, when the data are fitted using Eq. (5), which takes into account VCMA and self-heating effects, all quantities become RA independent. This means that STT switching parameters are intrinsically not RA dependent but their apparent RA dependence is due to an error from fitting t_p vs V_c assuming that STT is the only mechanism responsible for switching, without including contributions from VCMA and self-heating effects.

From Fig. 6(e), the fitting model of Eq. (5) predicts an RA-independent value of $E_b/I_{c0} \cong 0.1$ $k_BT/\mu A$. However, from the macrospin model of Eq. (1), taking $E_b = M_stH_kA/2$, $E_b/I_{c0} = \hbar\eta/(4e\alpha) \cong 1.8$ $k_BT/\mu A$, using the values in Table I. This 18-times discrepancy for E_b/I_{c0} is far greater than the aforementioned 3.5-times one for τ/α, despite the fact that both expressions, derived from Eq. (1), share the same physical parameters $\hbar\eta/(2e)$. The immediate cause of this is that the value $\Delta \cong 70$ obtained by fitting the experimental data using Eq. (5) [see Fig. 6(d)] is much smaller than the value $\Delta = 474$ obtained by calculating E_b using the parameter values in Table I for average $D = 90$ nm. Further explanations are beyond the physics of the macrospin model [23,25].

It is noted that the self-heating term $-\zeta V_c^2/RA'$ of Eq. (5) explicitly violates the assumption that E_b is a T-independent quantity, as is commonly implied by Arrhenius-type models such as the TA model in the case of Eq. (4) [26]. In Eq. (5), the parameter H_{k0} is the room T value rather than that at $T \rightarrow 0$ and $E_b \propto H_k$ will vary with T due to self-heating regardless of the presence of VCMA and STT effects. This implies that M_sH_k of the cell effectively has additional T dependence [25] besides that attributable solely to thermal fluctuations in the FL magnetization direction, which is otherwise treated by the denominator k_BT in the expression for Δ_{eff} [27]. This could result from the failure of the macrospin model to account for nonuniform (spin-wave mode) magnetization fluctuations.

IV. CONCLUSION

In conclusion, we point out that using the obtained values for τ/α, ϵ, and ζ, we find that STT and self-heating

contribute comparably to FL switching at RA10 and the latter is the dominant switching mechanism for larger RAs. As $\zeta = (R_{th}A)dH_c/dT$, higher $R_{th}A$ values should result in lower J_c. $R_{th}A$ values twice as high as those measured in our cells have been reported in the literature [16,28], which suggests that further reduction of J_c should be possible with thermal optimization of perpendicular MRAM cells. We point out that the self-heating effects described in this work are relevant for the design of practical memory applications operating in the read or write pulse time range of tens to hundreds of nanoseconds, as long as the thermal time-relaxation constant is of the order of a few nanoseconds or less, these being the values typically found in the literature [16,28].

---

[1] T. N. Theis and H.-S. P. Wong, The end of Moore's law: A new beginning for information technology, Comput. Sci. Eng. **19**, 41 (2017).

[2] M. Marjani, F. Nasaruddin, A. Gani, A. Karim, I. A. T. Hashem, A. Siddiqa, and I. Yaqoob, Big IoT data analytics: Architecture, opportunities, and open research challenges, IEEE Access **5**, 5247 (2017).

[3] J. S. Meena, S. M. Sze, U. Chand, and T. Y. Tsemg, Overview of emerging nonvolatile memory technologies, Nanoscale Res. Lett. **9**, 526 (2014).

[4] H.-S. P. Wong and S. Salahuddin, Memory leads the way to better computing, Nat. Nanotechnol. **10**, 191 (2015).

[5] D. Apalkov, B. Dieny, and J. M. Slaughter, Magnetoresistive random access memory, Proc. IEEE **104**, 1796 (2016).

[6] A. D. Kent and D. C. Worledge, A new spin on magnetic memories, Nat. Nanotechnol. **10**, 187 (2015).

[7] A. V. Khvalkovskiy, D. Apalkov, S. Watts, R. Chepulskii, R. S. Beach, A. Ong, X. Tang, A. Driskill-Smith, W. H. Butler, P. B. Visscher, D. Lottis, E. Chen, V. Nikitin, and M. Krounbi, Basic principles of STT-MRAM cell operation in memory arrays, J. Phys. D: App. Phys. **46**, 074001 (2013).

[8] J. Z. Sun, Spin-current interaction with a monodomain magnetic body: A model study, Phys. Rev. B **62**, 570 (2000).

[9] X. Wang, W. Zhu, Y. Zheng, Z. Gao, and H. Xi, Possible spin pumping effects on spin torque induced magnetization switching in magnetic tunneling junctions, IEEE Trans. Magn. **45**, 3414 (2009).

[10] Z. M. Zeng, P. Khalili Amiri, G. Rowlands, H. Zhao, I. N. Krivorotov, J.-P. Wang, J. A. Katine, J. Langer, K. Galatsis, K. L. Wang, and H. W. Jiang, Effect of resistance-area product on spin-transfer switching in MgO-based magnetic tunnel junction memory cells, Appl. Phys. Lett. **98**, 072512 (2011).

[11] G. Hu *et al.*, in *2017 IEEE International Electron Devices Meeting (IEDM)* (IEEE, San Francisco 2017), p. 38.3.1.

[12] J. Z. Sun, Resistance-area product and size dependence of spin-torque switching efficiency in CoFeB-MgO based magnetic tunnel junctions, Phys. Rev. B **96**, 064437 (2017).

[13] Y. Tserkovnyak, A. Brataas, and G. E. W. Bauer, Spin pumping and magnetization dynamics in metallic multilayers, Phys. Rev. B **66**, 224403 (2002).

[14] T. Maruyama, Y. Shiota, T. Nozaki, K. Ohta, N. Toda, M. Mizuguchi, A. A. Tulapurkar, T. Shinjo, M. Shiraishi, S. Mizukami, Y. Ando, and Y. Suzuki, Large voltage-induced magnetic anisotropy change in a few atomic layers of iron, Nat. Nanotechnol. **4**, 158 (2009).

[15] P. K. Amiri and K. L. Wang, Voltage-controlled magnetic anisotropy in spintronic devices, SPIN **2**, 1240002 (2012).

[16] C. Papusoi, R. Sousa, J. Herault, I. L. Prejbeanu, and B. Dieny, Probing fast heating in magnetic tunnel junction structures with exchange bias, New J. Phys. **10**, 103006 (2008).

[17] R. H. Koch, J. A. Katine, and J. Z. Sun, Time-Resolved Reversal of Spin-Transfer Switching in a Nanomagnet, Phys. Rev. Lett. **92**, 088302 (2004).

[18] Z. Li and S. Zhang, Thermally assisted magnetization reversal in the presence of a spin-transfer torque, Phys. Rev. B **69**, 134416 (2004).

[19] D. C. Worledge and P. L. Trouilloud, Magnetoresistance measurement of unpatterned magnetic tunnel junction wafers by current-in-plane tunneling, Appl. Phys. Lett. **83**, 84 (2003).

[20] P.-Y. Clement, C. Ducruet, C. Baraduc, M. Chshiev, and B. Dieny, Diffusive model of current-in-plane-tunneling in double magnetic tunnel junctions, Appl. Phys. Lett. **100**, 262404 (2012).

[21] N. Smith, M. J. Carey, and J. R. Childress, Measurement of Gilbert damping parameters in nanoscale CPP-GMR spin valves, Phys. Rev. B **81**, 184431 (2010).

[22] M. Goto, Y. Wakatake, U. Kalu Oji, S. Miwa, N. Strelkov, B. Dieny, H. Kubota, K. Yakushiji, A. Fukushima, S. Yuasa, and Y. Suzuki, Microwave amplification in a magnetic tunnel junction induced by heat-to-spin conversion at the nanoscale, Nat. Nanotechnol. **14**, 40 (2019).

[23] J. Z. Sun *et al.*, Spin-torque switching efficiency in CoFeB-MgO based tunnel junctions, Phys. Rev. B **88**, 104426 (2013).

[24] J. M. Shaw, S. E. Russek, T. Thomson, M. J. Donahue, B. D. Terris, O. Hellwig, E. Dobisz, and M. L. Schneider, Reversal mechanisms in perpendicularly magnetized nanostructures, Phys. Rev. B **78**, 024414 (2008).

[25] L. Thomas, G. Jan, S. Le, Y.-J. Lee, H. Liu, S. Zhu, J. Serrano-Guisan, R.-Y. Tong, K. Pi, D. Shen, R. He, J. Haq, Z. Teng, A. Rao, V. Lam, Y.-J. Wang, T. Zhong, T. Torng, and P.-K. Wang, in *2015 IEEE International Electron Devices Meeting (IEDM)* (IEEE, San Francisco, 2015), p. 26.4.1.

[26] S. Oh, S. Park, A. Manchon, M. Chshiev, J. Han, H. Lee, J. Lee, K. Nam, Y. Jo, Y. Kong, B. Dieny, and K. Lee, Bias-voltage dependence of perpendicular spin-transfer torque in asymmetric MgO-based magnetic tunnel junctions, Nat. Phys. **5**, 898 (2009).

[27] C. Zener, Classical theory of the temperature dependence of magnetic anisotropy energy, Phys. Rev. **96**, 1335 (1954).

[28] I. L. Prejbeanu, S. Bandiera, J. Alvarez-Hérault, R. C. Sousa, B. Dieny, and J.-P. Nozières, Classical theory of the temperature dependence of magnetic anisotropy energy, J. Phys. D: Appl. Phys. **46**, 074002 (2013).